Applied Surface Science 638 (2023) 158099

Contents lists available at ScienceDirect

Applied Surface Science

journal homepage: www.elsevier.com/locate/apsusc

Full Length Article

Multi-layered active sites attached in 1D/3D hierarchical conductive network promote dioxygen fragmentation

Yue Lu [a], Han Zhang [a,☆], Weichen Han [a], Jingang Zheng [a], Hao Huang [a], Lin Tao [a], Baigang An [a], Lixiang Li [a], Chengguo Sun [a,b,☆]

[a] School of Chemical Engineering, University of Science and Technology Liaoning, Anshan 114051, PR China
[b] School of Chemical Engineering, Nanjing University of Science and Technology, Nanjing 210094, PR China

ARTICLE INFO

Keywords:
Multi-layered active sites
Hemin
Oxygen intermediates
Dioxygen fragmentation

ABSTRACT

The sluggish kinetic process of oxygen conversion reaction directly limits the energy density of Zn-air batteries (ZABs), construction of multi-layered catalytic active sites to promote dioxygen fragmentation is an urgent need for high-performance ZABs. Herein, a bead-like 1D/3D hierarchical conductive network catalyst (Fe/Co-NC) is fabricated, where polypyrrole nanotubes served as skeleton, its surface was coated with polymerized Hemin which have the first active site and double propionic groups as the adsorption sites for the formation of second site precursor of ZIF-67. We defined the Fe/Co-N_x derived by pyrolysis dispersed in 1D/3D structure as multi-layered active sites. Fe/Co-NC catalyst exhibits excellent catalytic performance ($E_{1/2}$ = 0.86 V) and stability (the $E_{1/2}$ loses 0.21 mV after 5000 cycles). After assembling to ZABs, the results show an inspiring peak power density of 238.6 mW cm^{-2}, which is 1.8 times that of Pt/C catalyst. Density functional theory (DFT) indicates that multi-layered active sites can promoting dioxygen fragmentation rate − determining steps at higher limiting potential of 0.70 V. Partial density of states further demonstrates that multi-layered active sites with a downshift of the d-band center (-0.95 eV) weakens the adsorption of oxygen intermediates. Combined with conductivity calculations, density of states can reach higher levels, facilitating 4-electron transfer process.

1. Introduction

The limited reserves fossil fuels and increasingly serious environmental pollution problems have promoted the rapid demand and development of green, sustainable and clean energy. [1,2] Dioxygen (O_2) reactions are broadly regarded as the most promising electrochemistry conversion method because of its renewable resources and zero pollution. [3] Generally, the conversion of O_2 involves two reaction processes, dioxygen fragmentation (O_2 reduction reaction, ORR) and dioxygen formation (O_2 evolution reaction, OER); For example, Zn-air batteries can reduce O_2 into H_2O during the discharge process in the presence of cathode catalysts, which realize the conversion between chemical energy and electrical energy. [4] The discharge performance of the ZABs is affected by the rate-limiting processes of the O_2 reaction happened at the cathode catalyst. The kinetics of the dioxygen fragmentation is the rate-determining step during the discharging of Zn^{2+}, which is controlled by the influence of an efficient catalyst. High-loading Pt is required to overcome the kinetic sluggish kinetics of dioxygen fragmentation reaction with $4H^+/4e^-$ multi-step reactions. [5–6] However, the scarcity and instability of Pt-based catalysts become an obstacle for the large-scale commercial application ZABs catalysts. [7] Hence, designing low-cost, high-performance and stable platinum group metals (PGM) -free catalysts substitutes is at present an urgent problem to be solved. [8].

Among the cases reported in the literatures, transition metal-based N-doped porous carbon materials (M−NC, M = Fe, Co, Ni, etc.), [9] transition metal oxides [10] and other PGM-free catalysts have been studied as ORR catalysts. It is concluded that an ideal catalyst with high-efficiency ORR activity has two obvious advantages: i) the reactive active sites of catalysts have good ability to activate the O-O bond. ii) The catalyst should be conductive network-structured materials with high porosity, which facilitates mass transfer efficiency and diffusion of oxygen as well as rapid transfer of electrons. [11–12] In addition, according to the Sabatier principle, the dioxygen fragmentation performance is mainly determined by the adsorption-energy scaling relationship between the active sites and oxygen intermediates. [5,13]

☆ Corresponding authors.
E-mail addresses: hzhang0807@163.com (H. Zhang), sunyangguo2004@163.com (C. Sun).

https://doi.org/10.1016/j.apsusc.2023.158099
Received 3 June 2023; Received in revised form 16 July 2023; Accepted 24 July 2023
Available online 25 July 2023

The design of ideal M−NC catalyst should have the right amount of binding strength between oxygen-containing intermediates and active sites. Therefore, it is crucial to optimize the adsorption and desorption behavior of oxygenated intermediates during dioxygen fragmentation. [14] Previous studies have shown that except regulating the coordination environment of the active site by introducing heteroatoms and the introduction of bimetallic active sites is an effective way to synergistically adjust the adsorption energy of the d-band center and oxygen with the active site. This adjustment results in the elongation of the dioxygen bond length, thereby promoting the fragmentation of O_2. [15–17].

As we all know, the Fe-N_x species stand out as one of the most efficient active centers for oxygen conversion, which can effectively induce changes of local charge density and accelerate the process of O_2 adsorption and reduction. [3,18] However, the construction of Fe-N_x active site usually requires carbonization treatment, while the metal ions tends to form aggregates of metal nanoparticles, leading to the poor ORR performance and stability. [19] An effective method to alleviate the accumulation of metal ions is to achieve greater uniform dispersion through coordination protection between organic ligands and metal ions or pore-limiting effect of carbon structures. [20] For example, Mai et al. proposed a ZIF-mediated strategy to obtain catalysts with Co-N_x and Co nanocrystals monodisperse anchored on phenolic resin-derived carbon nanorods, which exhibited decent oxygen reduction performance in alkaline media. [21] Hemin as the most popular precursor of iron species, can relieve the Fe accumulation because the Fe^{3+} is located in the center of a highly conjugated planar structure with four pyrrole molecules coordination to allow the formation of uniform dispersion of Fe sites. [22] MOFs-based derivative materials are also important metal complex, such as ZIF-67 is an attractive of precursors with high nitrogen content, abundant hierarchical pores, and dispersed Co sites. It is also frequently used to construct metal active site centers. [23–25] However, large particles ZIF-67 cause the high resistance and stability of calcined catalyst. [26] One effective method is to address the issues by adding conductive additives and constructing conductive carriers. [27] Therefore, the construction of a special conductive network backbone with multi-layered active sites, achieve synergy of active sites is the key to the development for efficient ZABs.

Herein, we constructed a 1D/3D hybrid conductive electrocatalyst Fe/Co-NC, which features bead-like structure. The Hemin-coated PPy nanotubes (serve as the support skeleton) is characterized by a 1D conductive network and an Fe-N_x active site. It is worth mentioning that double propionic groups of Hemin serve as an effective adsorption site facilitates to trap Co^{2+}, this feature was exploited to introduce a 3D conductive network and Co-N_x active site. Upon carbonization, we achieved multi-layered active sites synergistic catalysis and porous 1D/3D conducting backbones act as a highway for fast electron and ion

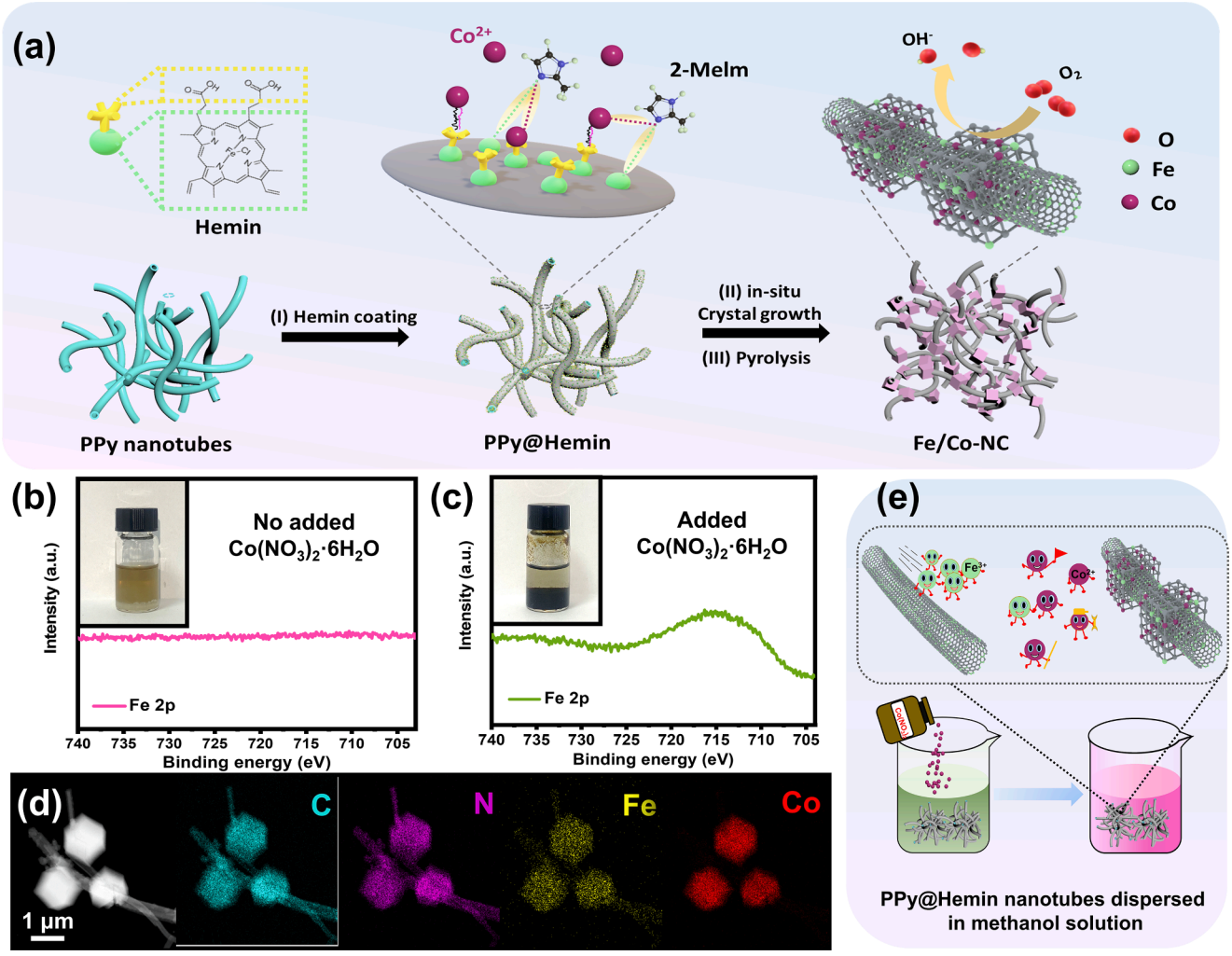

Fig. 1. (a) Schematic illustration of the Fe/Co-NC multi-layered active sites electrocatalyst. High-resolution XPS spectroscopy of Fe 2p of the formed precipitate by (b) adding or (c) not adding $Co(NO_3)_2{\cdot}6H_2O$ to the solution of methanol mixed with PPy@Hemin sample, the appropriate amount of NaOH solution was added to its centrifuged solution. (inset: Optical photographs of the precipitation formation). (d) HAADF-STEM images of PPy@Hemin/ZIF-67 and corresponding elemental maps of C, N, Fe and Co, respectively. (e) Schematic illustration of the diffusion of Fe ions into solution.

transport. The Fe/Co-NC catalyst exhibits highly efficient dioxygen fragmentation catalytic performance and superior stability in an alkaline medium, comparable to commercial Pt/C catalyst. Moreover, we demonstrate excellent electrochemical performance of assembled aqueous ZABs with Fe/Co-NC air cathodes that surpasses that of the Pt/C catalyst.

2. Results and discussion

The synthesis schematic diagram of multi-layered sites encapsulated in 1D/3D hierarchical conducting network backbone catalyst Fe/Co-NC is illustrated in Fig. 1**a.** Polypyrrole nanotubes were employed as the foundational skeleton in the first layer, its surface was subsequently coated with polymerized Hemin. Within the second layer, Hemin-derived Fe-N_x species acted as active sites. The double propionic groups of Hemin functioned as robust adsorption sites, exhibiting a strong affinity towards Co^{2+} ions. This strong binding interaction facilitated the growth of ZIF-67 in the third layer. Hemin-functionalized PPy linked cubic particles ZIf-67 together and effectively reduce interparticle resistance and aggregation. A bead-like 1D/3D hierarchical conducting network structure Fe/Co-NC catalyst with multi-layered sites was formed by calcination at 900 °C.

The morphologies of different catalysis were investigated by scanning and transmission electron microscope (SEM and TEM) measurements. Based on our previous work, [28] PPy nanotubes and PPy@Hemin composites were successfully fabricated as shown in **Fig. S1-2a, b**, the PPy surface changed to rough after coating Hemin. The results can also be demonstrated by Fourier transform infrared spectroscopy (FTIR) (**Fig. S3**). While providing Fe-N_x sites, Hemin can serve as a bridge between PPy and ZIF-67, the PPy nanotubes were functionalized with highly conjugated structural properties, and the strong polar group of double propionic groups contained effectively captured Co^{2+} for further formation of ZIF-67 nanocrystals. The successful preparation of PPy@Hemin/ZIF-67 sample was confirmed as shown in **Fig. S2c, d**. A smooth surface ZIF-67 (diamond-shaped 12-hedron, 900 nm approximately) was in-situ grown on the outer wall of PPy@Hemin and featured bead-like structure.

Interestingly, Fe element was not only dispersed on the surface of the nanotubes but also uniformly present in the ZIF-67 nanoparticles. This indicated that some Fe ions of PPy@Hemin were diffused into the solvent and replaced Co ions during the formation of ZIF-67 nanoparticles on the PPy@Hemin surface. This was further demonstrated by elemental mapping analysis (Fig. 1**d**), which visualized the existence and uniform distribution of C, N, Fe and Co elements in the PPy@Hemin/ZIF-67 nanobead material. The phenomenon of Fe ions diffusion was demonstrated by comparative experiments. $Co(NO_3)_2{\cdot}6H_2O$ was added to a methanolic solution containing PPy@Hemin samples that were homogeneously dispersed. The experimental conditions for ZIF-67 growth were simulated, and the resulting filtrate was obtained by centrifugation. To investigate the role of $Co(NO_3)_2{\cdot}6H_2O$ in the process, NaOH solution was dropwise added to both filtrates. The filtrate with Co $(NO_3)_2{\cdot}6H_2O$ added formed a brown precipitate, while the filtrate without the addition of $Co(NO_3)_2{\cdot}6H_2O$ produced a white precipitate (Fig. 1**b, c**). High-resolution XPS spectroscopy was used to analyze the resulting precipitates. The precipitate formed by the filtrate with Co $(NO_3)_2{\cdot}6H_2O$ addition showed the appearance of Fe 2p diffraction peaks, while the precipitate formed by the filtrate without Co $(NO_3)_2{\cdot}6H_2O$ addition did not detect any Fe element. This phenomenon indicates that the addition of Co salts led to the diffusion of Fe ions, which were introduced into ZIF-67 and substituted a portion of Co species due to the higher oxidizing properties of Co than those of Fe ions, via an anion exchange reaction. [29] The mechanism of Fe ion diffusion is depicted schematically in Fig. 1**e**. Additionally, similar elemental information of Fe was detected by XPS by adding other cobalt salts such as $CoCl_2{\cdot}6H_2O$, $CoSO_4$, and $Co(OAc)_2{\cdot}4H_2O$ as cobalt sources (**Fig. S4**).

The morphology of the multi-layered sites encapsulated in 1D/3D hierarchical conducting network backbone sample Fe/Co-NC was further analyzed. As shown in Fig. 2**a, b**, SEM and TEM images Fe/Co-NC catalyst inherited the PPy@Hemin/ZIF-67 uniform size and bead structure, except that the catalyst surface became rougher after calcination. Specifically, the existence of the many fine black dots that can be clearly observed on the Fe/Co-NC catalyst (Fig. 2**c**). Small clusters of Fe metal encapsulated on carbon nanotubes were observed. This suggests that high temperature calcination causes aggregation of Fe^{2+} in Hemin to form monomers. [30] They are covered by graphitic carbon layers with a lattice stripe of 0.341 nm (Fig. 2**d**). The result illustrates nanoparticles catalyzing graphitization on the surface of Fe/Co-NC, which observed graphite carbon area echoed the X-ray diffraction (XRD) result C (002) (Fig. 3**a**). High-resolution transmission electron microscopy (HR-TEM) images of the ZIF-67 particles in Fe/Co-NC sample demonstrate clearly resolved lattice stripe and calculated to be 0.205 nm (Fig. 2**e, f**), corresponding to the face-centered cubic metallic Co (111) (*JCPDS: no. 05–0806*). [31].

Fe/Co-NC sample with multi-layered active sites were successfully prepared and confirmed by XRD characterization (**Fig. S6a**). The XRD diffraction peak of the PPy@Hemin/ZIF-67 sample basically simulated of the ZIF-67, implying that ZIF-67 has successfully in-situ grown on the PPy@Hemin outer wall. It is consistent with the SEM and TEM information. Fig. 3**a** displayed all the diffraction peaks of Fe/Co-NC sample matching ZIF-67 disappeared, and new diffraction peaks appeared at 44.22°, 51.52° and 75.85°, corresponding to (111), (200) and (220) for a metallic Co, respectively. The lattice plane shows that the modification of Co nanoparticles on Fe/Co-NC, which is consistent with the peak position of Co-NC. No crystal signal of Fe species in XRD, which is consistent with the observation of morphological characterization. High-angle annular dark-field scanning TEM (HAADF-STEM) images and the corresponding elemental mapping images indicate that C, N, Fe and Co are homogeneously dispersed throughout the catalysts (Fig. 2**g**), which was consistent with the information of EDS spectrum (**Fig. S5**). This indicated that Fe species may be uniformly dispersed in a bead-like 1D/3D hierarchical conducting network backbone as single atoms or clusters. The presence of Fe oxides of Fe-NC sample may be attributed to being oxidized during the experiment. [22] The appearance of the C (002) peak in **Fig. S6b** illustrated the PPy@Hemin/ZIF-67 was converted to graphitized Fe/Co-NC-X (700–1000) by pyrolysis.

The graphitic degrees of the Fe/Co-NC catalysts were further investigated by Raman spectroscopy (Fig. 3**b**).Two obvious sharp peaks appear at 1340 cm^{-1} (D-band) and 1599 cm^{-1} (G-band), which can reflect the structure, defects and lattice properties of the samples. [32] The degree of carbon material defects is measured by the intensity ratio of the I_D/I_G. [33] The lower I_D/I_G (1.25) of Fe/Co-NC sample compared to Co-NC (1.45) and Fe-NC (1.40) samples implies that the construction of 1D/3D hierarchical conducting network backbone structure can enhance graphitization and improve conductivity. [34] In addition, the graphitization of the Fe/Co-NC samples were increased until calcination to 1000 °C (**Fig. S6c**). N_2 adsorption–desorption measurements of Fe/Co-NC were shown in **Fig. S6d-g** (**Table S1**). Fe/Co-NC-900 catalysis exhibits a large specific surface area of 278.7 $m^2\ g^{-1}$ and a smaller average pore size of 4.1 nm. Unique structural features of 1D/3D hierarchical conducting network-structured Fe/Co-NC catalyst not only exposed more active sites and fully wetted with the electrolyte, but also accelerated the mass transfer rate of electrons/ions and reduced the diffusion resistance. [32] Meanwhile, the surface area of Fe/Co-NC-1000 decreased to 181.7 $m^2\ g^{-1}$ with the average pore size of 6.5 nm, indicating that pore structure of the material was collapsed at 1000 °C. In addition, the results can also be confirmed by SEM (**Fig. S6h, i**). [35].

We further explored the chemical composition and states of the Fe/Co-NC catalysts with multi-layer active sites by X-ray photon spectroscopy (XPS). **Fig. S7** indicated that C, N, Fe, Co elements were also detected in Fe/Co-NC samples, corresponding to the results of mapping and EDS (Fig. 2**g, S5 and Table S2**). Meanwhile, the elemental information of NCNT, Fe-NC and Co-NC samples were displayed on **Fig. S8**.

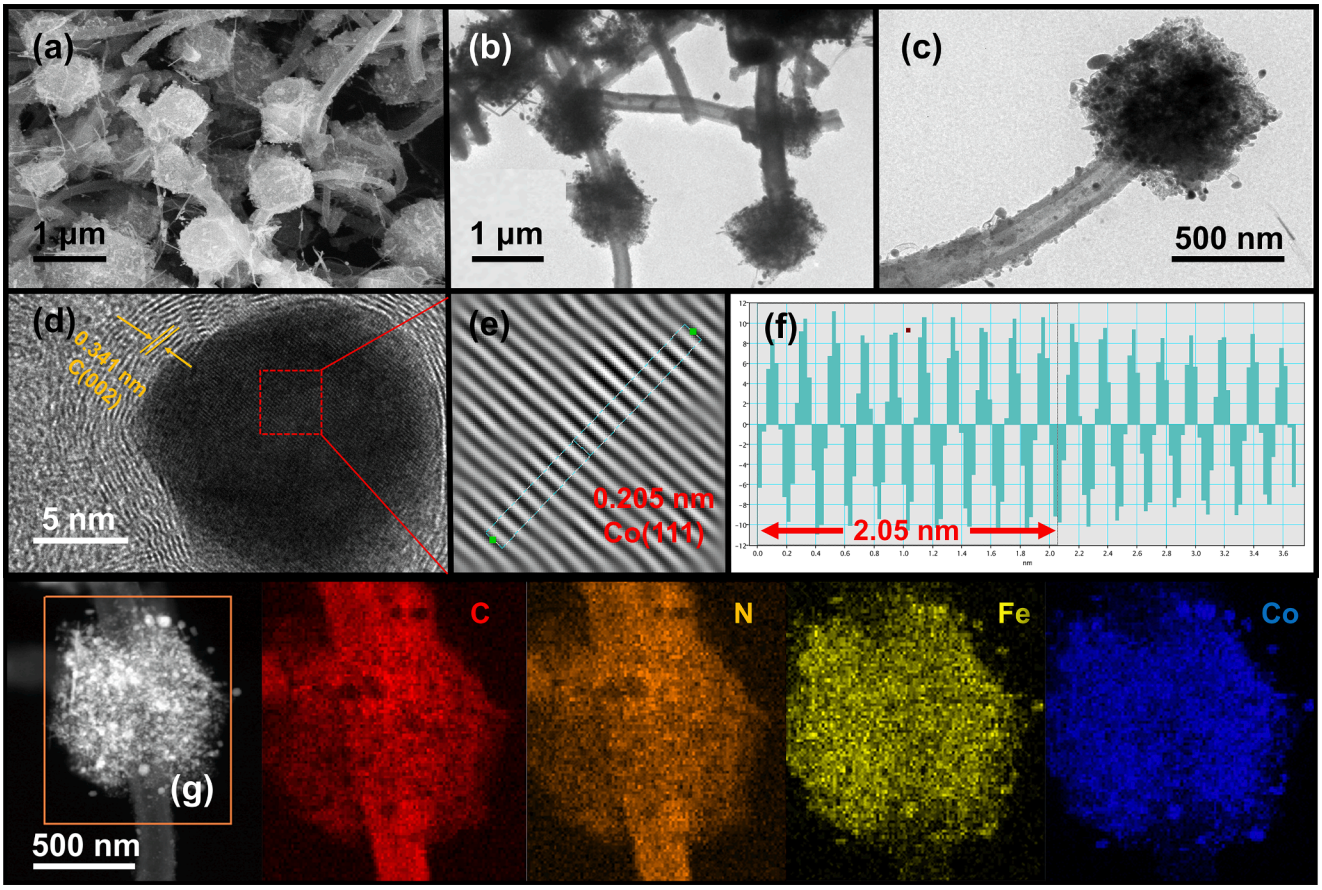

Fig. 2. (a) SEM images and (b, c) TEM images of Fe/Co-NC. (d, e) HR-TEM images of Fe/Co-NC. (f) Line profile analysis for Fe/Co-NC. (g) HAADF-STEM images of Fe/Co-NC and corresponding elemental maps of C, N, Fe and Co, respectively.

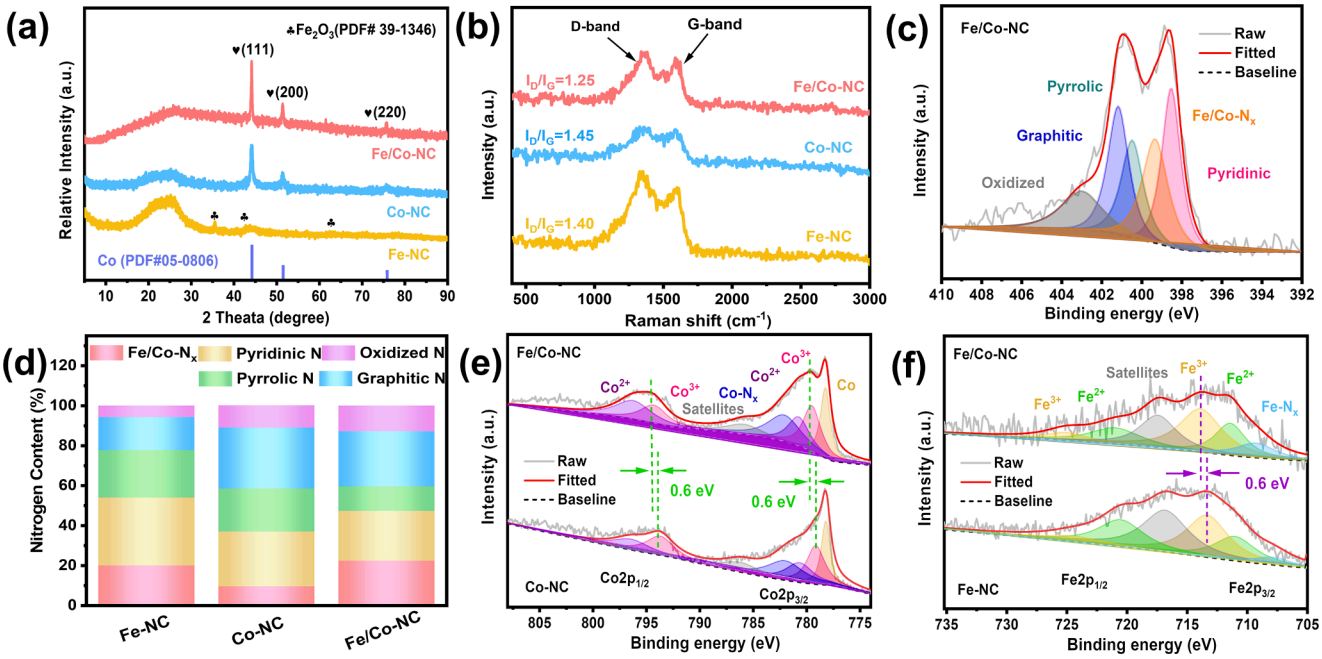

Fig. 3. (a) XRD patterns and (b) Raman spectra of Fe/Co-NC, Co-NC and Fe-NC samples. (c) High-resolution XPS spectroscopy of N 1s of Fe/Co-NC. (d) Nitrogen contents in Fe/Co-NC, Co-NC and Fe-NC of three different N configurations. (e) Co 2p and (f) Fe 2p XPS spectra of Fe/Co-NC, Co-NC and Fe-NC, showing the transfer of binding energy.

The high-resolution N 1 s spectra of Fe/Co-NC sample (Fig. 3**c**) can be fitted and deconvolved into Pyridine N, Pyrrole N, Graphite N, Graphite oxidized N, and Fe/Co-N_x species. [36–37] The relative content was summarized in **Table S3**. Fe/Co-based coordination compound precursor of the PPy@Hemin/ZIF-67 sample are decomposed after pyrolysis to form multi-layered active sites Fe-N_x and Co-N_x. For most catalysts, the coordination between the metal and the N atom is regarded as the effective active site of the ORR. [38] In comparison with the Fe-NC and Co-NC samples (**Fig. S9**), the Fe/Co-NC sample demonstrated the highest doping level and homogeneous Fe-N_x and Co-N_x active sites introduced (Fig. 3**d and Table S3**), which are expected to contribute significantly to the performance due to incorporating the advantages of multi-layered active sites Fe-N_x and Co-N_x. Furthermore, the Graphite N and Pyridine N were considered to promote the dioxygen fragmentation. The generation of Graphite N types can facilitate the adsorption of O_2 and promote the process of electron transfer during the ORR reaction, and the limit current density is improved. [39–40] The lone pair of electrons contained in Pyridine N causes the delocalized π orbit of the C framework to contain more electrons to enhance the basicity of the material and the π electrons are prone to nucleophilic attack on O_2. Higher content of Pyridine-N, Graphite-N and Fe/Co-N_x could endow Fe/Co-NC-900 catalyst with better ORR catalytic activity (**Fig. S10-11 and Table S4**).

The peak at 781.8 eV in the high-resolution spectrum Co $2p_{3/2}$ of Fe/Co-NC (Fig. 3**e**) was attributed to Co-N_x species. The doping effect of nitrogen was further proved by the analysis of Fe/Co-N_x sites in the N 1s spectrum and the presence of the Co-N_x sites was confirmed. In addition, the peak of Co 2p is resolved into five components: a doublet of Co $2p_{3/2}$ and Co $2p_{1/2}$ at 783.4 eV and 796.0 eV, respectively. The peaks represent the surface oxidation of Co^{2+}, the presence Co nanoparticles and peaks mixture of Co^{3+}, [41–42] which corresponds to the Co 2p spectral peak position of Co-NC. It has been reported that the Co-N_x species can facilitate the activation of the dioxygen molecular bond and reduce the onset potential for ORR. [15] The results show that Fe/Co-NC were exhibited that the highest Co-N_x contents in the Fe/Co-NC-X (700–1000) samples (**Fig. S12** and **Table S5**). The formation of Fe-N_x species of Fe/Co-NC sample in the corresponding high-resolution spectrum of Fe 2p was evidenced by peak at 708.1 eV (Fig. 3**f**).The four sub-bands 713.9, 725.0, 711.4 and 721.0 eV respectively represent the Fe^{3+} and Fe^{2+} of Fe $2p_{3/2}$ and Fe $2p_{1/2}$ orbital, which corresponds to the peak position of the Fe-NC sample. [43] The literature pointed out that Fe-N_x species can boost the reduction of intermediates, reducing O_2 to H_2O for the 4-electron pathway. [44] The high Fe-N_x contents (9.7%) of Fe/Co-NC (**Table S6**) was expected to significantly increase the ORR activity in Fe/Co-NC-X (700–1000) samples (**Fig. S13**).

In order to insight into the synergy and interplay between the multi-layered active sites Fe/Co-N_x of Fe/Co-NC sample, high-resolution XPS analysis was performed on different samples, as shown in Fig. 3**e, f**. Relative to isolated active site (Co-NC or Fe-NC), Fe/Co-NC sample exhibited energy shifts for binding energies of Co 2p and Fe 2p spectra. The obvious change from 779.07 eV (Co-NC) to 779.67 eV (Fe/Co-NC), a positive shift of about 0.6 eV for Co 2p, which represents the loss of electrons in Co relative to the original state. A positive energy transfer about 0.6 eV from 713.3 eV (Fe-NC) to 713.9 eV (Fe/Co-NC). It also indirectly proves the introduction of the multi-layered active sites (Fe/Co-N_x) changed the local electron density near the isolated active site (Co-N_x or Fe-N_x) with a synergistic effect. [37,45–46].

Based on the unique physical characterization information above, the dioxygen fragmentation performance of as-prepared materials was evaluated in alkaline media. The dioxygen fragmentation electrocatalytic capability of Fe/Co-NC sample was measured by cyclic voltammetry (CV) and rotating disk electrode (RDE) measurements. **Fig. S14a** shows the comparison with CV test curves of Fe/Co-NC samples collected under different aeration conditions (N_2-saturated/O_2-saturated) in 0.1 M KOH (scan rate of 50 mV s^{-1}). Obviously, a cathodic peak (0.82 V vs. RHE) was observed under O_2-saturated conditions, indicating an ORR reaction with O_2. [47] Compared to the other samples and different pyrolysis temperature catalysts, the CV test curves of Fe/Co-NC catalyst exhibited high-efficiency dioxygen fragmentation capability (**Fig. S15 and Table S7**). Linear sweep voltammograms (LSV) were tested using RDE in an O_2-saturated alkaline medium, Fig. 4**a** illustrates the polarization curves of Fe/Co-NC catalyst with a positive onset potential (E_{onset} = 1.01 V), the most positive half-wave potential ($E_{1/2}$ = 0.86 V) and the maximum limit current density (-5.21 mA cm^{-2}), which were substantially better than performance of Fe-NC, Co-NC, NCNT samples, and even surpassed the latest Pt/C catalyst (JM 20%) ($E_{1/2}$ = 0.82 V, -4.76 mA cm^{-2}). The RDE polarization curves of the different catalysts at 1600 rpm clearly observed that the worst performance was PPy-derived N-doped carbon nanotubes, which implied that conductive network is not the key for a superior catalytic performance of the dominant material. The electrochemical performance of the Fe-NC and Co-NC catalysts were similar, which are lower than those of Fe/Co-NC catalyst with the multi-layered active sites (the specific data is summarized in the **Table S8**). This implied that the electrocatalytic performance of material can be improved due to the isolated metal nitrogen of the comparison samples, but the maximum catalytic efficiency cannot be achieved. Highly efficient catalytic capability of Fe/Co-NC sample can be attributed to the synergistic effect Fe/Co-N_x multi-layered active sites and construction of 1D/3D hierarchical conducting network backbone structure, given to make the active sites of the catalyst more dispersed, shorter mass transfer distance, and enhanced electrocatalytic performance. Furthermore, the excellent kinetics of Fe/Co-NC sample could be further evidenced by the lowest Tafel slope (56 mV dec^{-1}) than Pt/C catalysis (88 mV dec^{-1}) and comparison samples (Fig. 4**b**). A small slope indicated that part of the electrode process in the hybrid zone is less hindered in the LSV polarization curve, so the smaller the applied potential, the greater the limit current density J, which is verified in Fig. 4**a**. Compared to the Fe-N_x or Co-N_x, the results proved that the synergy of Fe/Co-N_x multi-layered active sites could enhance the ORR activity. **Fig. S14b** displayed the kinetic process of Fe/Co-NC sample under the conditions of rotating disk electrodes at 400–2500 rpm. The LSV polarization curves showed that the increase in the limiting current density value was accompanied by an increase of revolutions of the working electrode. This phenomenon accounts for the reduction in the diffusion distance of O_2. The diffusion limiting current density displayed a straight curve in the 0.1 M KOH electrolyte solution, which exhibited that O_2 undergoes a 4-electron oxygen reduction reaction on Fe/Co-NC catalyst. The Koutecky-Levich (K-L) plots of the four catalysts were linearly fitted to similar parallel lines and indicated the first-class dynamics kinetics towards dioxygen fragmentation. Moreover, the kinetic current density (J_k@0.85 V) of Fe/Co-NC was calculated to be 4.99 mA cm^{-2}, which are 1.81, 6.3 and 3.46 times larger than the J_k values of Pt/C, Co-NC and Fe-NC samples, respectively (Fig. 4**c**). Fig. 4**d** radar plot shows the most outstanding performance of Fe/Co-NC catalyst compared with other comparison catalysts. Furthermore, we compared catalytic behavior of Fe/Co-NC with previously reported bimetallic catalysts, which demonstrated that the Fe/Co-NC exhibits outstanding ORR activity due to the synergistic interactions between the Fe/Co-N_x multi-layered active sites and construction of 1D/3D hierarchical conducting network backbone structure (**Table S9**).

Subsequently, the oxygen reduction electron transfer number n and HO_2^- yield of Fe/Co-NC, Pt/C catalyst and contrast samples were tested and calculated by rotating ring disk electrode (RRDE). Fig. 4**e and Fig. S14c** observed that Fe/Co-NC catalyst has the smallest HO_2^- yield of about 1.37% and consistent with the Pt/C 4-electron transfer number, which indicates that the Fe/Co-NC catalyst is typical the 4-electron process reduces O_2 to H_2O. In addition, the electrocatalytic stability of the catalyst and methanol tolerance are also important indicators of cathode materials. The sensitivity of Fe/Co-NC and Pt/C catalysts to methanol were investigated in the same test conditions by chronoamperometry (**Fig. S14d**). It is worth mentioning that the current

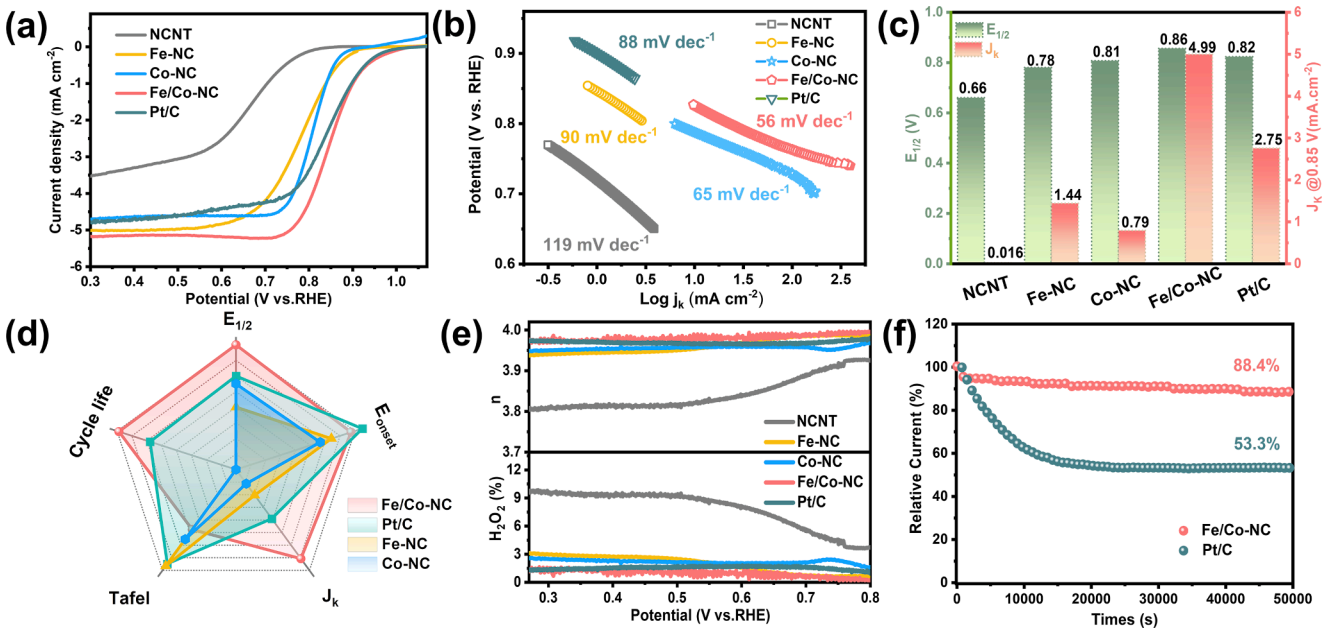

Fig. 4. Electrocatalytic performance evaluation of different catalysts in O_2-saturated 0.1 M KOH solution. (a) LSV polarization curves of different catalysts at 1600 rpm. (b) Corresponding Tafel plots obtained from the RDE polarization curves. (c) Comparision of $E_{1/2}$ and J_k at 0.85 V (vs. RHE) of different catalysts. (d) Radar plot on performance comparison with different ORR catalysts. (e) H_2O_2 yield and electron transfer number (n) of different catalysts. (f) Chronoamperometric measurements of Fe/Co-NC and Pt/C.

density of the Pt/C catalyst immediately responded tremendously. Afterwards, it gradually decreases and tends to be gentle when 5 M methanol was added in 600 s. However, a negligible slight change in the current density J of the Fe/Co-NC sample was observed, which clarified that it has better methanol resistance. The electrochemical stability of Fe/Co-NC sample was also tested using chronoamperometry measurement as shown in Fig. 4**f**. Fe/Co-NC held long-term stability with 88.4% (compared with 53.3% for Pt/C) retention of initial current after 50000 s. Thus, the Fe/Co-NC also exhibited better ORR stability. In addition, the cycle stability of the Fe/Co-NC sample also was assessed by the accelerated durability test (ADT) as shown in **Fig. S14e, f,** the $E_{1/2}$ value of the Fe/Co-NC catalyst hardly changed, which was lower than the change value of $E_{1/2}$ for Pt/C catalyst (15 mV of negative shift). The HR-TEM, XRD, and XPS of Fe/Co-NC after 5000 cycles were characterized to further study the stability of the catalyst. [48] The detailed results are shown in **Fig. S16,** which revealed that the samples after long-cycle testing showed similar properties to the as-prepared Fe/Co-NC, including the morphology, phase and component, suggesting that the Fe/Co-NC was stable with no significant change during the catalytic ORR process. The Fe/Co-N_x sites at 399.2 eV, the Co-N_x species at 781.8 eV and the Fe-N_x species at 711.4 eV are all well-preserved after the long-term catalysis, indicating that Fe/Co-NC catalyst active sites have good stability. The excellent electrochemical stability of the Fe/Co-NC sample was attributed to its stable 1D/3D hierarchical conducting network backbone structure and stable bonding between PPy@Hemin and ZIF-67.

We further determined the electrochemical surface area (ECSA) of different catalysts by recording CV curves from 0.95 to 1.05 V vs. RHE at different scan rates. The various rates of CV curves for different rates for Fe/Co-NC, Fe-NC and Co-NC samples are shown in **Fig. S17a-c**, respectively. The ECSA of catalysts is shown in **Fig. S17d**. The ECSA of Fe/Co-NC sample is 7.94 mF cm^{-2}, which is higher than that of Fe-NC (0.51 mF cm^{-2}) and Co-NC (5.51 mF cm^{-2}). Those results indicate that Fe/Co-NC catalyst has a large electrochemical surface area containing a high number of active sites. The above results illustrate the Fe/Co-NC catalysts possess excellent ORR activity.

To further confirm the role of the multi-layered active sites Fe/Co-N_x, the SCN^- poison experiments was carried out. It is well known that thiocyanate anions bind strongly and selectively to metals in the form of nanoparticles and atomic dispersions, blocking access to the metal active center and decreasing the electrocatalytic activity. [49–50] **Fig. S18** manifesting that the $E_{1/2}$ of Fe/Co-NC catalyst was negatively shifted by 48 mV and the electrode diffusion limit current density liquid was significantly reduced after the introduction of 10 mM KSCN. After activation under O_2-saturated conditions the SCN^- on the Fe/Co-NC was replaced by oxygen bulging and the ORR activity was almost restored to its original performance. [51] It suggests that the multi-layered active sites Fe/Co-N_x play an important part in catalytic ORR. It is known that metal-N active sites and dispersed Co atoms dispersed N-doped graphitic carbon layers can be formed in Co-MOF derivatives during high temperature pyrolysis. [52] To further verify whether the excellent catalytic capacity of the Fe/Co-NC sample is attributed to the synergistic catalytic effect of multi-layered active sites or the Co atom particles. We immersed the Fe/Co-NC samples in 6 M hydrochloric acid for 3 days at 100 °C in order to etch out the Co particles and noted as E-Fe/Co-NC **(Fig. S19a)**. SEM images of E-Fe/Co-NC revealed that the bead-like hybrid conductive network structure was still maintained after HCl etching **(Fig. S19b, c)**. As shown in **Fig. S19d-e,** most of the remaining Co element exists in the form of Co-N_x, and only small amount of Co particles embedded in the thick carbon layers. **Table S10** reveals that the weight percentage of Co element in the E-Fe/Co-NC sample is 1.2%, which is only 10% of the Co content in the Fe/Co-NC sample by using inductively coupled plasma emission spectrometer (ICP). This indicated that a large number of Co metal particles in the E-Fe/Co-NC sample were effectively removed. **Fig. S19f** points out that weak characteristic peaks of metallic Co for E-Fe/Co-NC were appeared and compared with Fe/Co-NC, indicative of a low content of crystalline cobalt particles. The results of RDE and RRDE electrochemical tests on E-Fe/Co-NC and Fe/Co-NC catalysts show that they have similar electrocatalytic activities **(Fig. S19g-i)**. Therefore, it can be inferred that the synergistic effect of the multi-layered active sites Fe/Co-N_x is the main reason for the excellent performance.

In addition, the Fe/Co-NC samples were explored for electrochemical activity at different pyrolysis temperatures. The dioxygen fragmentation performance of the catalyst is optimized by annealing with different temperature. The surface active-material of the catalyst and the local

structure of carbon (including porosity and graphitization degree) may be changed because of the pyrolysis temperature, implying that could affect the ORR activity. [53] The RDE polarization curves of Fe/Co-NC-X (700–1000) samples were shown in **Fig. S20a** which reveals that the multi-layered-sites Fe/Co-NC-900 sample was exhibited high-efficiency catalytic performance (**Table S7**). The K-L plots of different samples at -0.45 V were fitted with reflected good linearity and near parallelism, which indicated the first-class dynamical kinetics towards dioxygen fragmentation. The ORR electron transfer number of the Fe/Co-NC-X (700–1000) catalyst at -0.45 V were calculated. The ORR electron transfer number (3.95) of Fe/Co-NC-900 is closest to the 4-electron transfer mechanisms of Pt/C catalyst (**Fig. S20b**), which is the dominant ORR reaction pathway. The kinetic current density (J_k@0.85 V) and $E_{1/2}$ of Fe/Co-NC-X (700–1000) were shown in **Fig. S20c,** it is noteworthy that Fe/Co-NC-900 has the largest J_k@0.85 V and $E_{1/2}$, which were considered to the most excellent performance and illustrated the optimal heat treatment temperature of Fe/Co-NC sample approximately 900 °C.

To investigate the role of multi-layered active sites synergistic effect in the superior dioxygen fragmentation catalytic activity of Fe/Co-NC sample, we performed DFT calculations using the computational hydrogen electrode model. [54] Generally, the ORR reaction process consists of four basic reaction steps, in which ORR generates *OOH by adsorption of O_2 and further reduces to *O and *OH. Based on the structural and electrochemical analysis, three different models, Fe/Co-NC, Co-NC, and Fe-NC, were constructed (Fig. 5**e, S21**). Adsorption configurations and the corresponding adsorption Gibbs free energies (eV) of the reaction intermediates *OOH, *O, and *OH were analyzed. Besides, it shows that the diagrams of adsorption configurations and the corresponding adsorption Gibbs free energies (eV) of the reaction intermediate *OOH, *O, and *OH. It can be found that the catalytic cycle was initiated by adsorption of oxygen onto catalyst surface, followed by 4e$^-$ reduction steps, which accepted 1e$^-$, respectively. As shown in Fig. 5**a-c**, the three different model catalysts possess consistent downhill energy paths at an external U = 0 V in alkaline media, indicating that all electron transfer steps can be performed spontaneous exothermic processes. [55] Among which, calculated and compared from the free energies of each step, the rate-determining steps were both the fourth reduction step (desorption of the *OH intermediate) due to the small Gibbs free energy. Generally, there is a maximum U (denoted as the limiting potential) to ensure that the ORR steps remain exothermic. [38] Fe/Co-NC model displays a maximum limiting potential of 0.70 V, superior to Fe-NC (0.49 V) and Co-NC (0.68 V) models (Fig. 5**a-c**). In addition, the Co clusters model was further constructed to calculate the free energy of the corresponding ORR process. The result showed that the maximum limiting potential of the Co clusters model was 0.59 V, which was lower than that of the Fe/Co-NC model (**Fig. S22a, b**). They prove that Fe/Co-NC has a lower overpotential. The synergistic catalytic effect of the multi-layered Fe and Co active sites was mainly responsible for its outstanding activity towards the ORR. Further insights were gained by comparing the partial density of states (PDOS), as the d-band center is highly associated with the metal adsorbate interaction. [56] In Fig. 5**d, a** downshift of the d-band center was observed in Fe/Co-NC (-0.95 eV) compared with Fe-NC (-0.55 eV) and Co-NC (-0.80 eV), resulting in fewer electrons being occupied in the antibonding orbital. [57] This demonstrates the positive influence of multi-layered active sites synergistic effect, thus Fe/Co-NC has optimal catalytic activity. All models showed metallic characters with the density of states (DOS) crossing over the Fermi level. Fe/Co-NC had a higher DOS (5.8 /eV) near the Fermi level, superior to Fe-NC (4.0 /eV) and Co-NC (3.9 /eV), proving enhanced electron mobility and higher activity. Therefore, these account for the high dioxygen fragmentation activity of multi-layered active sites synergistic effect. In the meantime, the proposed catalytic mechanism of dioxygen fragmentation with Fe/Co-NC sample is depicted in Fig. 5**e**. By comparing the free energy of the ORR process between the two different models constructed Fe/Co*–NC (O_2 is adsorbed to the Co atom) and Fe*/Co-NC (O_2 is adsorbed to the Fe atom). (**Fig. S22c, d**) O_2 molecule is first adsorbed on the Fe active sites with electron-rich, and then it gradually transfers to intermediates with the increase of the applied potential and finally to OH^-. The synergy of multi-layered Fe/Co-N_x sites can effectively modify the electronic filling state of the d-band center, facilitate the desorption process of oxygen species intermediates, and decrease the energy of controlling steps, thus ensuring good dioxygen fragmentation performance.

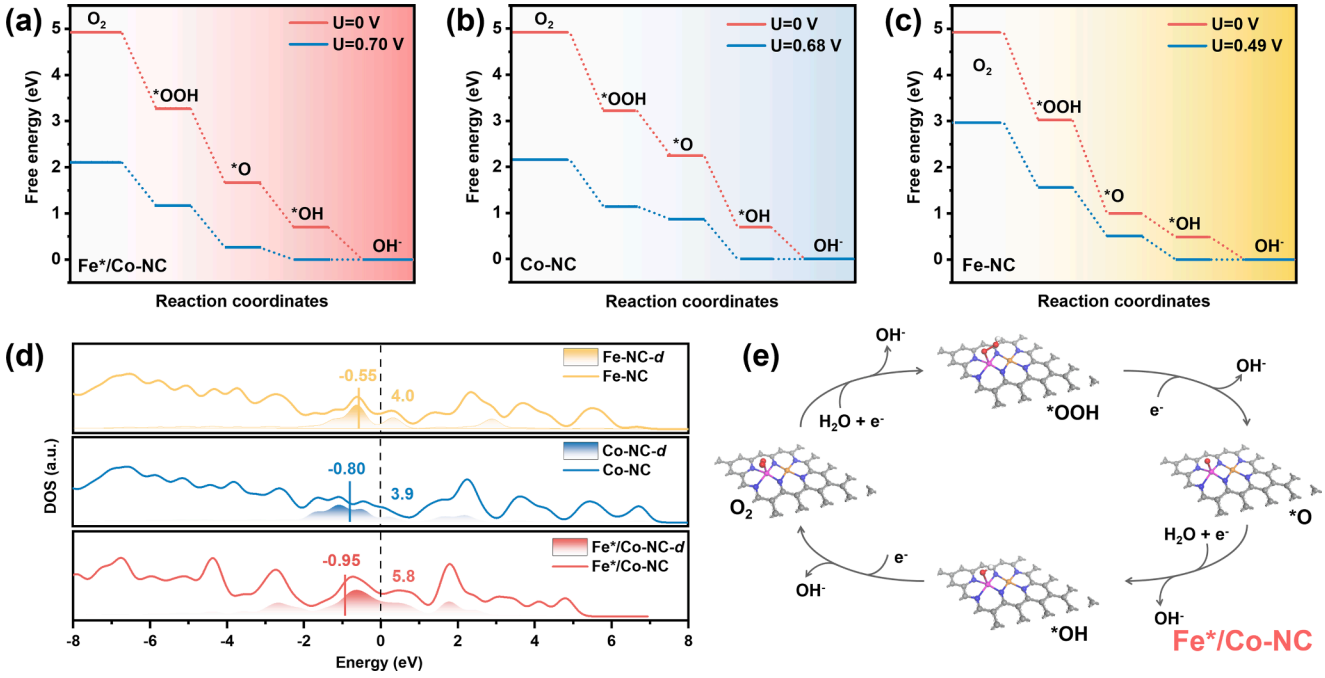

Fig. 5. Free energy diagram for ORR processes of (a) Fe*/Co-NC, (b) Co-NC, and (c) Fe-NC. (d) The density of state, partial density of states, and d-band center for Fe-NC, Co-NC, and Fe*/Co-NC. (e) Scheme of the transition states in mechanism of ORR at Fe*/Co-NC from DFT. (blue, gray, white, red, orange, and pink balls represent the N, C, H, O, Co, and Fe atoms, respectively.).

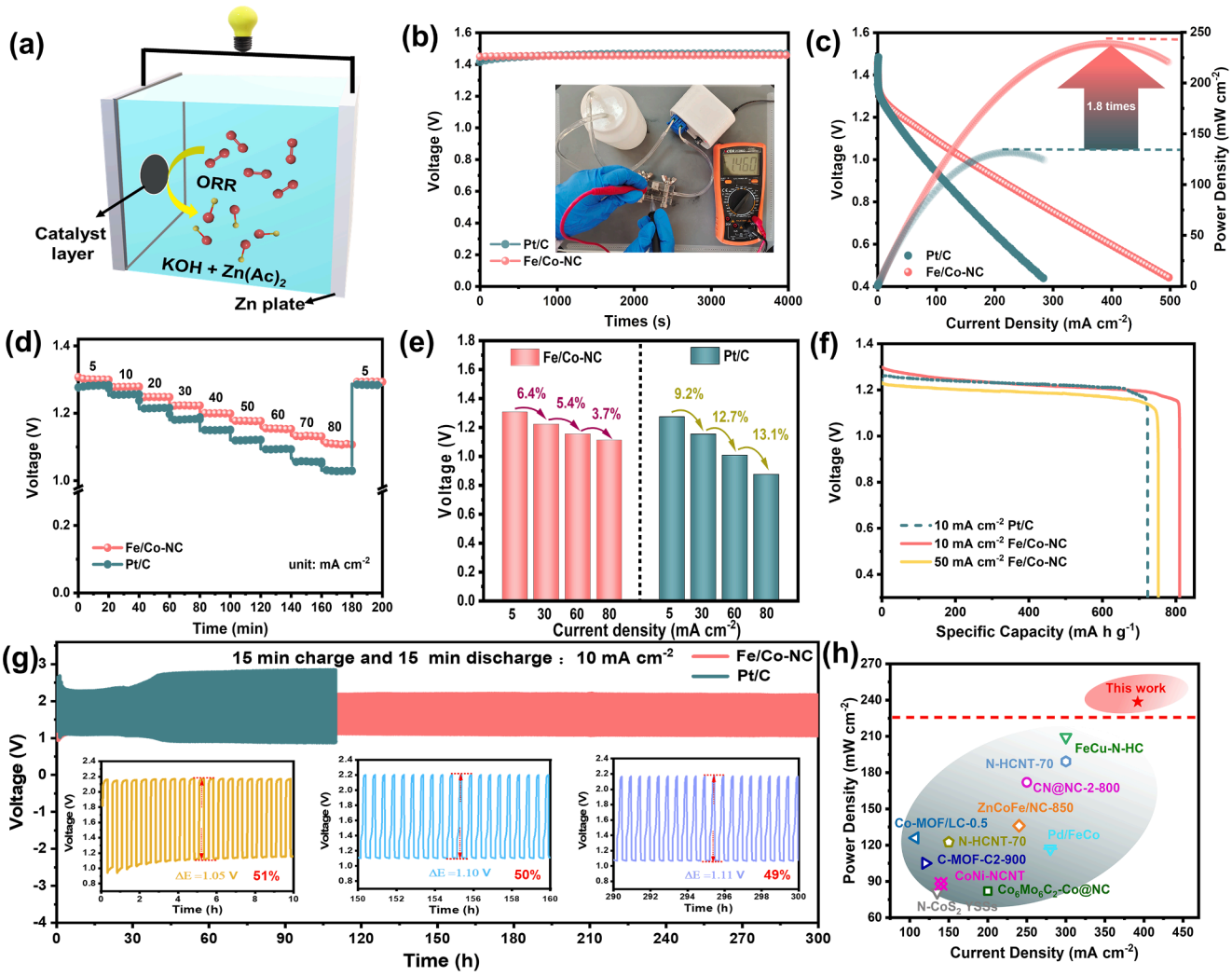

Fig. 6. (a) Schematic of aqueous ZABs using Fe/Co-NC as air cathode. (b) Open-circuit potential versus time curves for the battery based on Fe/Co-NC and Pt/C as an air cathode. inset: photograph of a ZABs with an open-circuit voltage of 1.46 V. (c) Polarization and power density curves of ZABs using Pt/C and Fe/Co-NC catalyst (mass loading, 1 mg cm^{-2}) and 6 M KOH electrolyte (scan rate, 5 mV s^{-1}). (d) Discharge curves of ZABs at different current densities from 5 to 80 mA cm^{-2} using Pt/C and Fe/Co-NC as ORR catalyst and (e) histograms of a ZABs discharge at different current densities. (f) Galvanostatic discharge curves at 10 and 50 mA cm^{-2} discharging rate. The specific capacity is normalized by the mass of the consumed Zn anode. (g) Long-term cycling performance at a current density of 10 mA cm^{-2} with Fe/Co-NC and Pt/C catalyst. (h) The performance compared with recently reported performances of ZABs cathode electrocatalysts.

In order to characterize the optimal dioxygen fragmentation performance, the aqueous Zn-air battery (ZABs) is assembled based on Fe/Co-NC powder coated on carbon paper as the positive electrode (Fig. 6**a**). As shown in Fig. 6**b**, the Fe/Co-NC catalyst delivers an open-circuit voltage (OCV) up to 1.46 V after 4000 s, which is similar to OCV of Pt/C catalyst (~1.46 V). The output power density of ZABs is evaluated by recording the discharge polarization curve. Fig. 6**c** shows that Fe/Co-NC sample obtained a peak power density of 238.6 mW cm^{-2} at the current density corresponding to 391.9 mA cm^{-2}. It is 1.8 times that of Pt/C catalyst (corresponding to 131.8 mW cm^{-2} at 221.7 mA cm^{-2}), which explains the Fe/Co-NC catalyst for ZABs has excellent output performance. In addition, Fe/Co-NC sample has a very small voltage drop in constant current discharge measurement at a current density from 5 to 80 mA cm^{-2}. The discharge will be reversible to recover once the current density is reduced to 5 mA cm^{-2}, indicating that excellent discharge rate performance (Fig. 6**d, e**). The discharge specific capacity of the ZABs with Fe/Co-NC catalyst was tested at 5, 10, 20, and 50 mA cm^{-2} (Fig. 6**f and S23a**). When normalized to the consumed Zn mass at 5 and 10 mA cm^{-2}, the specific capacity of ZABs based on Fe/Co-NC sample is 819 mA h g_{Zn}^{-1} and 810 mA h g_{Zn}^{-1}, which exceed the specific capacity of Pt/C sample as the cathode is 723 mA h g_{Zn}^{-1} (at 10 mA cm^{-2}). Even at a large discharge current density, it maintains 792 mA h g_{Zn}^{-1} (at 20 mA cm^{-2}), 752 mA h g_{Zn}^{-1} (at 50 mA cm^{-2}) corresponds to 96.6% and 91.7% utilization of the calculated theoretical capacity, reflecting the superior discharge ability. The charge–discharge polarization diagram (**Fig. S23b**) reflected that Fe/Co-NC catalyst possesses a smaller gap value compared with Pt/C catalyst. Moreover, the Nyquist plots also suggest a small charge transfer resistance of Fe/Co-NC catalyst (**Fig. S23c**), revealing the lower charge transfer resistance. [58] The cyclic discharge ability was further investigated at 10 mA cm^{-2} with a recurrent galvanostaticpulse for 15 min of discharge followed by 15 min of charge (Fig. 6**g**). The battery driven by Fe/Co-NC demonstrates superior cycling stability compared to Pt/C catalysis. For the Fe/Co-NC cathode, the voltage decay is only 0.06 V and its energy efficiency reaches an ultra-stable level of 49% after 300 h of testing, reflecting the superior dischargeability. Two ZABs in series can light LED for a testing period of at least 2 days (**Fig. S23d**). Moreover, the performance compared with recently reported performances of ZABs cathode electrocatalysts (Fig. 6**h**, **Table S11**) once again proves the potential application of Fe/Co-NC catalyst in ZABs. Based on these results, the multi-layered active sites synergistically optimize the catalytic activity and conductivity in Fe/Co-NC catalysts, resulting in outstanding

performance. The bead-like structure provides both carbon and nitrogen sources, while double propionic groups of Hemin serve as the adsorption site for the in-situ growth of ZIF-67, providing multi-layered active sites and reducing electrical resistance and aggregation between ZIF-67 nanoparticles. Moreover, the porous 1D/3D hierarchical conducting network backbone offers sufficient exposed area for reaction sites and shortens the transport path of ions and electrons, ensuring the catalyst's stability.

3. Conclusions

In summary, an efficient and durable electrocatalyst was fabricated for the dioxygen fragmentation by encapsulating multi-layered active sites Fe/Co-N_x in a 1D/3D hierarchical conducting network of N-doped cubic carbon particles and carbon nanotubes (Fe/Co-NC). PPy nanotubes as a conductive framework are functionally encapsulated through the conjugation of Hemin, the double propionic groups act as an adsorption site for the formation of ZIF-67 precursor with the second site. This results in a robust and porous conductive network structure with highly dispersed multi-layered active sites that exhibit significant catalytic activity towards dioxygen fragmentation, as demonstrated by an E_{onset} of 1.01 V and $E_{1/2}$ of 0.86 V, as well as negligible variations in durability and methanol tolerance in the alkaline medium. We assembled aqueous ZABs with the synthesized catalysts, which exhibit remarkable energy density and specific capacity compared to Pt/C catalyst. The excellent electrochemical activity of the catalyst is attributed to the synergistic contribution of the multi-layered active sites Fe/Co-N_x that promote the 4-electron reaction of dioxygen fragmentation. Moreover, the bead-like 1D/3D hierarchical conducting network structure of Fe/Co-NC provides additional active sites and facilitates the ion–electron transport process, thereby enhancing the electrocatalytic performance. This novel structure with its special features, high stability and dioxygen fragmentation catalytic activity, holds great promise for use in diverse energy conversion and storage systems.

CRediT authorship contribution statement

Yue Lu: Investigation, Data curation, Writing – original draft. **Han Zhang:** Supervision, Project administration, Funding acquisition. **Weichen Han:** Resources. **Jingang Zheng:** Formal analysis. **Hao Huang:** Data curation. **Lin Tao:** Methodology, Funding acquisition. **Baigang An:** Supervision, Project administration, Funding acquisition. **Lixiang Li:** Supervision, Project administration. **Chengguo Sun:** Writing – review & editing, Supervision, Funding acquisition.

Declaration of Competing Interest

The authors declare that they have no known competing financial interests or personal relationships that could have appeared to influence the work reported in this paper.

Data availability

Data will be made available on request.

Acknowledgements

The authors gratefully acknowledge financial supported by the National Natural Science Foundation of China (11972178, 21701077, 51972156 and 22109061), the Nature Science Foundation of Liaoning Province (2022-BS-283), the Talent Project of Revitalizing Liaoning (2020LNQN17) and Technology Liaoning Project Grants (601010326). We also appreciate Dr. Lin Tao's help and contribution in the theoretical calculation part of the article with the Youth Fund of the Education Department of Liaoning Province (LJKQZ20222324).

Appendix A. Supplementary material

Supplementary data to this article can be found online at https://doi.org/10.1016/j.apsusc.2023.158099.

References

[1] S. Chandrasekaran, D. Ma, Y. Ge, L. Deng, H. Zhang, Electronic structure engineering on two-dimensional (2D) electrocatalytic materials for oxygen reduction, oxygen evolution, and hydrogen evolution reactions, Nano Energy 77 (14) (2020), 105080.
[2] J. Xue, Y. Li, J. Hu, Nanoporous bimetallic Zn/Fe–N–C for efficient oxygen reduction in acidic and alkaline media, J. Mater. Chem. A 8 (15) (2020) 7145–7147.
[3] A. Wc, B. Py, A. Zl, A. Yg, A. Yq, A. Xx, L.C. Xin, C. Wb, C. Kw, A. Qx, Boosting defective carbon by anchoring well-defined atomically dispersed metal-N_4 sites for ORR, OER, and Zn-air batteries, Appl. Catal. B 260 (2019) 118198.
[4] J. Zhang, T. Zhang, J. Ma, Z. Wang, X. Gong, ORR and OER of Co–N codoped carbon-based electrocatalysts enhanced by boundary layer oxygen molecules transfer, Carbon 172 (2021) 556–568.
[5] H. Sun, M. Wang, S. Zhang, S. Liu, X. Shen, T. Qian, C. Yan, Boosting oxygen dissociation over bimetal sites to facilitate oxygen reduction activity of zinc-air battery, Adv. Funct. Mater. 31 (4) (2020) 2006533.
[6] N. Shang, C. Wang, X. Zhang, S. Gao, Y. Gao, Atomically Dispersed Iron on Nitrogen-decorated Carbon for High-performance Oxygen Reduction and Zinc-Air Batteries, Chem. Eng. J. 426 (44) (2020), 127345.
[7] Y. Zhao, H.M. Zhang, Y. Zhang, M. Zhang, J. Yu, H. Liu, Z. Yu, B. Yang, C. Zhu, J. Xu, Leaf-like 2D nanosheet as efficient oxygen reduction reaction catalyst for Zn-air battery, J. Power Sources 434 (15) (2019), 226717.1-226717.7.
[8] Y. Zhu, Z. Zhang, Z. Lei, Y. Tan, N. Cheng, Defect-enriched hollow porous Co-N-doped carbon for Oxygen Reduction Reaction and Zn-Air Batteries, Carbon 167 (2020) 188–195.
[9] X. Liu, L. Wang, G. Zhang, F. Sun, H. Fu, Zinc Assisted Epitaxial Growth of N-Doped CNTs-Based Zeolitic Imidazole Frameworks Derivative for High Efficient Oxygen Reduction Reaction in Zn-Air Battery, Chem. Eng. J. 414 (2020), 127569.
[10] Y. Zhu, X. Liu, S. Jin, H. Chen, W. Lee, M. Liu, Y. Chen, Anionic defect engineering of transition metal oxides for oxygen reduction and evolution reactions, J. Mater. Chem. A 7 (11) (2019) 5875–5897.
[11] J. Wang, Z. Huang, W. Liu, C. Chang, H. Tang, Z. Li, Y. Li, Design of N-coordinated dual-metal sites: A stable and active Pt-free catalyst for acidic oxygen reduction reaction, J. Am. Chem. Soc. 139 (48) (2017) 17281–17284.
[12] P. Yin, T. Yao, Y. Wu, L. Zheng, Y. Lin, W. Liu, Y. Li, Single cobalt atoms with precise N-coordination as superior oxygen reduction reaction catalysts, Angew. Chem. 128 (36) (2016) 10958–10963.
[13] H.F. Wang, C. Tang, Q. Zhang, A review of precious-metal-free bifunctional oxygen electrocatalysts: Rational design and applications in Zn air batteries, Adv. Funct. Mater. 28 (46) (2018) 1803329.
[14] J.H. Zagal, M.T. Koper (Eds.), Reactivity descriptors for the activity of molecular MN4 catalysts for the oxygen reduction reaction, Angew. Chem. Int. 55 (47) (2016) 14510–14521.
[15] H. Li, Y. Wen, M. Jiang, Y. Yao, H. Zhou, Z. Huang, J. Li, S. Jiao, Y. Kuang, S. Luo, Understanding of neighboring Fe-N_4-C and Co-N_4-C dual active centers for oxygen reduction reaction, Adv. Funct. Mater. 31 (22) (2021) 2011289.
[16] L.X. Shidong Li, J. Li, Z. Chen, W. Zhang, J. Zhu, R. Yu, F. Liu, S. Lee, Y.Z. Liang Zhou, L. Mai, Tuning structural and electronic configuration of Fe-N_4 via external S for enhanced oxygen reduction reaction, Energy Environ. Mater. 6 (3) (2022) e12560.
[17] Z. Chen, G. Zhang, Y. Wen, N. Chen, W. Chen, T. Regier, J. Dynes, Y. Zheng, S. Sun, Atomically Dispersed Fe-Co Bimetallic Catalysts for the Promoted Electroreduction of Carbon Dioxide, Nano-micro letters 14 (1) (2022) 25.
[18] X. Wang, Y. Jia, X. Mao, D. Liu, W. He, J. Li, J. Liu, X. Yan, J. Chen, L. Song, Edge-rich Fe− N_4 active sites in defective carbon for oxygen reduction catalysis, Adv. Mater. 32 (16) (2020) 2000966.
[19] Z. Lu, J. Chen, W. Wang, W. Li, M. Sun, Y. Wang, X. Wang, J. Ye, H. Rao, Electrocatalytic, Kinetic, and Mechanism Insights into the Oxygen-Reduction Catalyzed Based on the Biomass-Derived FeOx@ N-Doped Porous Carbon Composites, Small 17 (19) (2021) 2007326.
[20] J. Huo, L. Lu, Z. Shen, Y. Liu, J. Guo, Q. Liu, Y. Wang, H. Liu, M. Wu, G. Wang, A rational synthesis of single-atom iron–nitrogen electrocatalysts for highly efficient oxygen reduction reaction, J. Mater. Chem. A 8 (32) (2020) 16271–16282.
[21] Qiang Yu, Jiantao Li, Ruohan Yu, Jinsong Wu, Shibo Xi, Xinyuan Li, Nuo Xu, Liang Zhou, ZIF-mediated anchoring of Co species on N-doped carbon nanorods as an efficient cathode catalyst for Zn-air batteries, Energy Environ. Mater. 6 (3) (2023) e12389.
[22] L. Zhiwei, W. WenLi, L. Wenjin, Mengmeng Sn, W. Yanying, W. Xianxiang, R. Hanbing, Electrocatalytic, kinetic, and mechanism insights into the oxygen-reduction catalyzed based on the biomass-derived FeOx@N-doped porous carbon composites, Small 17 (19) (2021) 2007326.1–2007326.10.
[23] J. Zhang, Y. Chen, Y. Liu, X. Liu, S. Gao, Self-catalyzed growth of Zn/Co-N-C carbon nanotubes derived from metal-organic frameworks as efficient oxygen reduction catalysts for Zn-air battery, Sci. China Mater. 65 (3) (2022) 653–662.
[24] W. Li, X. Guo, P. Geng, M. Du, Q. Jing, X. Chen, G. Zhang, H. Li, Q. Xu, P. Braunstein, Rational Design and General Synthesis of Multimetallic Metal-

Organic Framework Nano-Octahedra for Enhanced Li–S Battery, Adv. Mater. 33 (45) (2021) 2105163.
[25] C. Gao, Z. Jiang, P. Wang, J. Lr, Y. Zhang, Y. Yue, Metal-Organic Framework Glass Anode with an Exceptional Cycling-Induced Capacity Enhancement for Lithium Ion Batteries, Adv. Mater. 34 (10) (2022) 2110048.
[26] B. Li, K. Igawa, J. Chai, Y. Chen, Y.J.E.S.M. Zong, String of pyrolyzed ZIF-67 particles on carbon fibers for high-performance electrocatalysis, Energy Storage Mater. 25 (2020) 137–144.
[27] T.Y. Ma, S. Dai, M. Jaroniec, S.Z. Qiao, Metal–organic framework derived hybrid Co_3O_4 carbonporous nanowire arrays as reversible oxygen evolution electrodes, J. Am. Chem. Soc. 136 (39) (2014) 13925–13931.
[28] Y. Lu, H. Zhang, S. Liu, C. Li, C. Sun, Hemin-Based Conjugated Effect Synthesis of Fe-N/CNT Catalysts for Enhanced Oxygen Reduction, New J. Chem. 45 (15) (2021) 6940–6949.
[29] X. Zhang, F. Yan, X. Ma, C. Zhu, Y. Wang, Y. Xie, S.L. Chou, Y. Huang, Y. Chen, Regulation of morphology and electronic structure of FeCoNi layered double hydroxides for highly active and stable water oxidization catalysts, Adv. Energy Mater. 11 (48) (2021) 2102141.
[30] J. Guo, X. Yan, Q. Liu, Q. Li, X. Xu, L. Kang, Z. Cao, G. Chai, J. Chen, Y. Wang, The Synthesis and Synergistic Catalysis of Iron Phthalocyanine and Its Graphene-based Axial Complex for Enhanced Oxygen Reduction, Nano Energy 46 (2018), 347-335.
[31] Z. Hu, Z. Guo, Z. Zhang, M. Dou, F. Wang, Bimetal Zeolitic Imidazolite Framework-Derived Iron-, Cobalt- and Nitrogen-Codoped Carbon Nanopolyhedra Electrocatalyst for Efficient Oxygen Reduction, ACS Appl. Mater. Interfaces 10 (15) (2018) 12651–12658.
[32] Q. Zhou, Z. Zhang, J. Cai, B. Liu, Y. Zhang, X. Gong, X. Sui, A. Yu, L. Zhao, Z. Wang, Template-guided synthesis of Co nanoparticles embedded in hollow nitrogen doped carbon tubes as a highly efficient catalyst for rechargeable Zn-air batteries, Nano Energy 71 (2020), 104592.
[33] S. Zago, M. Bartoli, M. Muhyuddin, G.M. Vanacore, P. Jagdale, A. Tagliaferro, C. Santoro, S. Specchia, Engineered biochar derived from pyrolyzed waste tea as a carbon support for Fe-NC electrocatalysts for the oxygen reduction reaction, Electrochim. Acta 412 (2022), 140128.
[34] Y. Wang, K. Li, R. Cheng, Q. Xue, F. Wang, Z. Yang, P. Meng, M. Jiang, J. Zhang, C. Fu, Enhanced electronic interaction between iron phthalocyanine and cobalt single atoms promoting oxygen reduction in alkaline and neutral aluminum-air batteries, Chem. Eng. J. 450 (2022), 138213.
[35] J. Guo, C.Y. Lin, Z. Xia, Z. Xiang, A pyrolysis-free covalent organic polymer for oxygen reduction, Angew. Chem. Int. Ed. 57 (38) (2018) 12567–12572.
[36] Z. Zhan, J. Yu, S. Li, X. Yi, J. Wang, S. Wang, B. Tan, Ultrathin Hollow Co/N/C Spheres from Hyper-Crosslinked Polymers by a New Universal Strategy with Boosted ORR Efficiency, Small 19 (16) (2023) 2207646.
[37] R. Dun, X. He, J. Huang, W. Wang, Y. Liu, L. Li, B. Lu, Z. Hua, J. Shi, Atomically Dispersed Fe/Co Dual Sites Electrocatalysts Derived from Covalent Triazine Frameworks for Boosting the Oxygen Reduction, J. Mater. Chem. A 11 (11) (2023) 5902–5909.
[38] D. Wang, H. Xu, P. Yang, X. Lu, J. Ma, R. Li, L. Xiao, J. Zhang, M. An, Fe–N_4 and Co–N_4 dual sites for boosting oxygen electroreduction in Zn–air batteries, J. Mater. Chem. A 9 (23) (2021) 13678–13687.
[39] Z. Hu, Z. Zhang, Z. Li, M. Dou, F. Wang, One-step conversion from core-shell metal-organic framework materials to cobalt and nitrogen codoped carbon nanopolyhedra with hierarchically porous structure for highly efficient oxygen reduction, ACS Appl. Mater. Interfaces 9 (19) (2017) 16109–16116.
[40] W.-J. Niu, Y.-Y. Yan, R.-J. Li, W.-W. Zhao, J.-L. Chen, M.-J. Liu, B. Gu, W.-W. Liu, Y.-L. Chueh, Identifying the impact of Fe nanoparticles encapsulated by nitrogen-doped carbon to Fe single atom sites for boosting oxygen reduction reaction toward Zn-air batteries, Chem. Eng. J. 456 (2023), 140858.
[41] L. Song, H. Fan, X. Fan, H. Gong, T. Wang, J. He, A simultaneous phosphorization and carbonization strategy to synthesize a defective Co_2P/doped-CNTs composite for bifunctional oxygen electrocatalysis, Chem. Eng. J. 435 (2022), 134612.
[42] T. Yu, X. Cao, R. Song, L. Li, X. Dong, J. Li, X. Wang, X. Zhou, N. Yuan, J. Ding, MOF-derived FeCo-NC@ Co_2P-NC as a high-performance bifunctional electrocatalyst for rechargeable Zn-air batteries, J. Alloy. Compd. 939 (2023), 168679.
[43] L. Li, L. Zhang, Z. Nie, W. Ma, N. Li, T. Wågberg, G. Hu, Tailoring charge reconfiguration in dodecahedral Co_2P@ carbon nanohybrids by triple-doping engineering for promoted reversible oxygen catalysis, J. Mater. Chem. A 10 (40) (2022) 21659–21671.
[44] F. Zhang, X. Liu, Y. Chen, M. Tian, T. Yang, J. Zhang, S. Gao, Ordered mesoporous carbon fiber bundles with high-density and accessible Fe-N_X active sites as efficient ORR catalysts for Zn-air batteries, Chin. Chem. Lett. 34 (10) (2023) 108142.
[45] C. Zhou, S. Zhao, H. Meng, Y. Han, Q. Jiang, B. Wang, X. Shi, W. Zhang, L. Zhang, R. Zhang, RuCoOx nanofoam as a high-performance trifunctional electrocatalyst for rechargeable zinc-air batteries and water splitting, Nano Lett. 21 (22) (2021) 9633–9641.
[46] Z.-Y. Mei, S. Cai, G. Zhao, Q. Jing, X. Sheng, J. Jiang, H. Guo, Understanding electronic configurarions and coordination environment for enhanced ORR process and improved Zn-Air battery performance, Energy Storage Mater. 50 (2022) 12–20.
[47] C. Ji, T. Zhang, P. Sun, P. Li, J. Wang, L. Zhang, Y. Sun, W. Duan, Z. Li, Facile preparation and properties of high nitrogen-containing Fe/Co/N co-doped three-dimensional graphene bifunctional oxygen catalysts for zinc air battery, Int. J. Hydrogen Energy 48 (67) (2023) 26328–26340.
[48] Y. Liu, Z. Li, L. Wang, L. Zhang, X. Niu, Tunable Fe/N co-doped 3D porous graphene with high density Fe-Nx sites as the efficient bifunctional oxygen electrocatalyst for Zn-air batteries, Int. J. Hydrogen Energy 46 (74) (2021) 36811–36823.
[49] X. Yang, D. Xia, Y. Kang, H. Du, F. Kang, L. Gan, J. Li, Unveiling the axial hydroxyl ligand on Fe–N_4–C electrocatalysts and its impact on the pH-dependent oxygen reduction activities and poisoning kinetics, Adv. Sci. 7 (12) (2020) 2000176.
[50] D. Xia, X. Yang, L. Xie, Y. Wei, W. Jiang, M. Dou, X. Li, J. Li, L. Gan, F. Kang, Direct growth of carbon nanotubes doped with single atomic Fe–N_4 active sites and neighboring graphitic nitrogen for efficient and stable oxygen reduction electrocatalysis, Adv. Funct. Mater. 29 (49) (2019) 1906174.
[51] S. Wang, P. Sun, N. Li, J. Wang, L. Zhang, W. Duan, Z. Li, The catalytic performance enhanced via π-electron cloud interaction of polymerized cobalt phthalocyanine/3D-graphene as bifunctional oxygen catalysts for Zn-air battery, J. Power Sources 556 (2022).
[52] H. Huang, S. Zhou, C. Yu, H. Huang, J. Zhao, L. Dai, J. Qiu, Rapid and energy-efficient microwave pyrolysis for high-yield production of highly-active bifunctional electrocatalysts for water splitting, Energ. Environ. Sci. 13 (2) (2020) 545–553.
[53] Z. Ma, L. Xu, L. Liu, L. Wang, X. Zhang, A. Kong, Bio-inspired chitosan-heme-vitamin B12-derived Fe–Co bimetallic-doped mesoporous carbons for efficiently electro-activating oxygen, Dalton Trans. 48 (7) (2019) 2338–2344.
[54] J.K. Nørskov, J. Rossmeisl, A. Logadottir, L. Lindqvist, J.R. Kitchin, T. Bligaard, H. Jónsson, Origin of the Overpotential for Oxygen Reduction at a Fuel-Cell Cathode, J. Phys. Chem. B 108 (46) (2004) 17886–17892.
[55] D. Xie, D. Yu, Y. Hao, S. Han, G. Li, X. Wu, S. Peng, Dual-Active Sites Engineering of N-Doped Hollow Carbon Nanocubes Confining Bimetal Alloys as Bifunctional Oxygen Electrocatalysts for Flexible Metal-Air Batteries, Small 17 (10) (2021) 3007239.
[56] L. Tao, D. Dastan, W. Wang, P. Poldorn, X. Meng, M. Wu, H. Zhao, H. Zhang, L. Li, B. An, Metal-decorated InN monolayer senses N_2 against CO_2, ACS Appl. Mater. Interfaces 15 (9) (2023) 12534–12544.
[57] Y. He, L. Tao, J. Li, M. Wu, P. Poldorn, D. Dastan, S. Abbasi, S. Nie, X. Yin, Q. Wang, Atomic-level insights into selective adsorption of H_2 and CO on SnO_2/CoO heterojunctions, Mater. Today Nano 22 (2023) 100334.
[58] Y. Liu, J. Bao, Z. Li, L. Zhang, S. Zhang, L. Wang, L. Xu, Large-scale defect-rich iron/nitrogen co-doped graphene-based materials as the excellent bifunctional electrocatalyst for liquid and flexible all-solid-state zinc-air batteries, J. Colloid Interface Sci. 607 (2) (2022) 1201–1214.